Faculty Research, Scholarly, and Creative Activity

4-1-2020

# An observational case study of synergies between an intense heat wave and the urban heat island in Beijing

Ning An
*China Meteorological Administration*

Jingjing Dou
*China Meteorological Administration*

Jorge E. González-Cruz
*City College of New York*

Robert D. Bornstein
*San Jose State University*, robert.bornstein@sjsu.edu

Shiguang Miao
*China Meteorological Administration*

*See next page for additional authors*

## Recommended Citation

Ning An, Jingjing Dou, Jorge E. González-Cruz, Robert D. Bornstein, Shiguang Miao, and Lin Li. "An observational case study of synergies between an intense heat wave and the urban heat island in Beijing" *Journal of Applied Meteorology and Climatology* (2020): 605-620. https://doi.org/10.1175/JAMC-D-19-0125.1

Authors

Ning An, Jingjing Dou, Jorge E. González-Cruz, Robert D. Bornstein, Shiguang Miao, and Lin Li

# An Observational Case Study of Synergies between an Intense Heat Wave and the Urban Heat Island in Beijing

NING AN,[a,b] JINGJING DOU,[a] JORGE E. GONZÁLEZ-CRUZ,[c] ROBERT D. BORNSTEIN,[a,d]
SHIGUANG MIAO,[a] AND LIN LI[e]

[a] *Institute of Urban Meteorology, China Meteorological Administration, Beijing, China*
[b] *College of Global Change and Earth System Science, Beijing Normal University, Beijing, China*
[c] *Department of Mechanical Engineering, City College of New York, New York, New York*
[d] *Department of Meteorology and Climatology, San Jose State University, San Jose, California*
[e] *Beijing Meteorological Observation Center, Beijing, China*

## ABSTRACT

The focus of this study is an intense heat episode that occurred on 9–13 July 2017 in Beijing, China, that resulted in severe impacts on natural and human variables, including record-setting daily electricity consumption levels. This event was observed and analyzed with a suite of local and mesoscale instruments, including a high-density automated weather station network, soil moisture sensors, and ground-based vertical instruments (e.g., a wind profiler, a ceilometer, and three radiometers) situated in and around the city, as well as electric power consumption data and analysis data from the U.S. National Centers for Environmental Prediction. The results show that the heat wave originated from dry adiabatic warming induced by the dynamic downslope and synoptic subsidence. The conditions were aggravated by the increased air humidity during subsequent days, which resulted in historically high records of the heat index (i.e., an index representing the apparent temperature that incorporates both air temperature and moisture). The increased thermal energy and decreased boundary layer height resulted in a highly energized urban boundary layer. The differences between urban and rural thermal conditions throughout almost the entire boundary layer were enhanced during the heat wave, and the canopy-layer urban heat island intensity (UHII) reached up to 8°C at a central urban station at 2300 local standard time 10 July. A double-peak pattern in the diurnal cycle of UHIIs occurred during the heat wave and differed from the single-peak pattern of the decadal average UHII cycles. Different spatial distributions of UHII values occurred during the day and night.

## 1. Introduction

A heat wave is an excessively hot period over consecutive days. Prolonged exposure to high temperatures can lead to heat-related illness, which results in increased morbidity and mortality (Braga et al. 2002; Patz et al. 2005). These heat-wave episodes can have severe social, environmental, and economic impacts and can cause a reduction in primary productivity (Ciais et al. 2005), a high risk of forest fires (Parente et al. 2018), and excessive consumption of electricity and water (Valor et al. 2001; Daniel et al. 2018). Studies have shown that heat waves are becoming more intense, lasting longer, and occurring more often globally against the background of global warming (Meehl and Tebaldi 2004; Sun et al. 2014; González et al. 2019).

The health impacts of heat waves are directly connected to high near-surface air temperatures and humidity (Davis et al. 2016; Chen 2017). Urban areas are particularly vulnerable under heat waves due to the urban heat island (UHI) effect, a phenomenon in which urban built-up areas experience warmer temperatures than the surrounding rural areas (Oke 1982). The UHI effect mainly results from the alteration of land surfaces with built materials such as asphalt and concrete, which have significantly different thermal bulk properties and surface radiative properties than natural land cover. In addition, anthropogenic heat emissions generated by human activities from buildings, transportation, and human metabolism play an important role in contributing to the UHI effect (Oke 1982; Stewart and Oke 2012; Iamarino et al. 2012).

In addition to high temperatures, high humidity can exacerbate the effects of heat waves on humans

*Corresponding author*: Shiguang Miao, sgmiao@ium.cn

(Karl and Knight 1997; Fischer et al. 2012). High humidity decreases the human body's efficiency in discharging heat through evaporative cooling (perspiration), which leads to increases in the body's internal temperature (Sherwood and Huber 2010). Therefore, when studying extreme heat days, the "heat index" is often used (Cristo et al. 2007; Ding and Qian 2011), which normally considers both air temperature and humidity (Steadman 1979a, 1984). However, urban areas are generally expected to have a lower air humidity than rural areas because of reduced evaporation from asphalt and concrete surfaces (Clark et al. 1985).

Over the past 30 years, the speed and scale of urbanization in Beijing have been unprecedentedly high (United Nations 2014; Jacobson et al. 2015). Surface land-use changes and anthropogenic emissions induced by the process of urbanization are changing meteorological conditions (e.g., temperature, wind, humidity, and precipitation), boundary layer structures, and surface energy budgets in Beijing (Miao et al. 2009; Yu et al. 2013; Dou et al. 2015).

The rapid pace of urbanization and the increasing risk of severe summer heat against the background of global warming highlight the importance of studying the interaction between heat waves and UHIs. The synergy between heat waves and the UHI effect has been addressed in numerous studies based on both observational analysis and model simulations. Amplified UHIs during heat waves have been documented in many cities across the world (Basara et al. 2010; Li and Bou-Zeid 2013; Founda and Santamouris 2017; Ramamurthy et al. 2017; Ortiz et al. 2018b; S. Jiang et al. 2019; Rizvi et al. 2019). Such synergistic effects between UHIs and heat waves have been attributed to the contrasting responses of urban and rural surface energy budgets to heat waves. For example, the incoming shortwave radiation and longwave radiation received in urban areas amplifies the energy storage in the built surfaces with the additional effects of increased sensible heat fluxes from the surfaces and from anthropogenic emissions (Li et al. 2015; Ao et al. 2019).

However, some studies investigating large collections of cities have found that there is not significant amplification of the UHIs (Ramamurthy and Bou-Zeid 2017; Zhao et al. 2018) or even reduced UHIs (Scott et al. 2018) during heat waves under some circumstances, which are linked to factors such as the physical sizes of cities, climate backgrounds, and weather conditions. Exacerbated UHIs during heat waves are more obvious in big cities and are not obvious in small cities (Ramamurthy and Bou-Zeid 2017). Cities in temperate climates have significant synergy effects, while those in arid regions have shown no discernible synergistic effects

(Zhao et al. 2018). Meteorological conditions (e.g., cloud and wind speeds) also have an impact on UHIs (Morris et al. 2001). Clear skies and low vapor pressure generally result in stronger UHI than cloudy skies and moist weather conditions because urban areas receive more solar radiation under clear skies, and rural areas can cool faster through emitted longwave radiation in low vapor conditions (Hardin et al. 2018; Eastin et al. 2018). The most reduced UHI was found under moist weather conditions (Scott et al. 2018). Wind speed is usually lower during heat waves because of accompanying surface high pressure (Ackerman and Knox 2012); lower wind speed leads to reduced advective cooling effect, and thus is expected to amplify the UHIs (Oke 1982; Li and Bou-Zeid 2013). Li et al. (2016) further found out that during the daytime period of heat waves, the urban wind speed is generally enhanced compared to the rural wind speed and leads to greater sensible heat flux in an urban zone, which can amplify the UHIs.

Despite these apparent large body of work on UHIs under heat waves, these studies are generally based on a few representative stations for single cities or model simulations, and most do not focus on the spatial features of interactions between urbanization and heat waves. In addition, few studies have addressed the differences in thermal conditions between urban and rural areas in the entire boundary layer during heat waves.

High-density automated weather stations (AWSs) have been established in both urban and rural areas in Beijing in the last few decades. On the basis of observations from these stations, the variations and distributions of UHIs have been elaborated (Miao et al. 2009; Yang et al. 2013; Zhang et al. 2015; K. Wang et al. 2017). However, such works did not explain how heat waves impact the spatial distributions of UHIs or how UHIs may affect temperature patterns during heat-wave events in Beijing.

The Study of Urban Impacts on Rainfall and Fog/Haze (SURF) field campaign has been ongoing in Beijing, China, and the surrounding area since 2015. SURF employs various sensors, including radiometers, lidar, radar, towers, and aircraft sensors, at multiple urban and rural stations (Liang et al. 2018). These observations provide us with the opportunity to study the evolution of the thermal and dynamic vertical structures of heat waves and extend the study of the thermal conditions between rural and urban areas from the canopy layer to the boundary layer.

From 9 to 13 July 2017, an intense heat-wave event occurred in Beijing. According to the Beijing Emergency Medical Center, the number of emergency services for
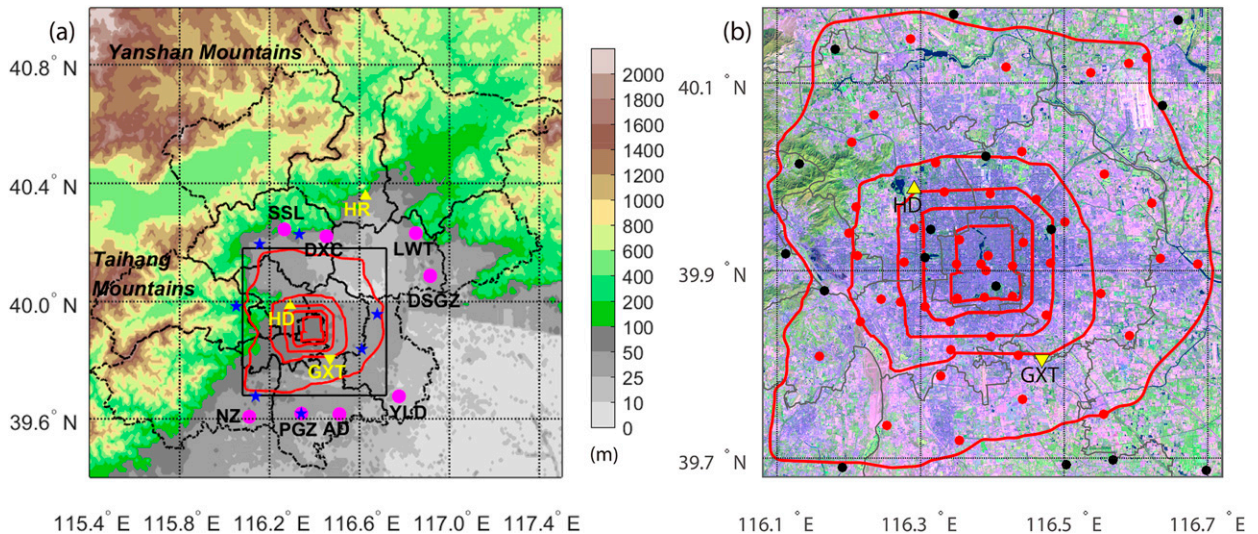
FIG. 1. (a) The topography of Beijing (m; color bar), city districts (dash–dotted lines), the study area (black-outlined rectangle), and ring roads (red lines). The locations of several stations are marked. Pink dots refer to the eight selected rural stations. Blue pentagrams refer to the seven soil moisture observation stations around the study area. The yellow inverted triangle indicates Guanxiangtai (GXT) station, and the two yellow triangles refer to Haidian (HD) and Huairou (HR) stations. (b) Distribution of the 67 automated weather stations (red and black dots) over different land-use types (the image is from Landsat-TM on 22 Sep 2009), including built-up areas (purple), green spaces (green), and water bodies (blue) in the study area. The red dots are the 51 selected urban stations.

heat stroke was unusually high during 10–13 July. This heat wave had a maximum electric power load demand that reached a historical new record of 22.54 million kW on 13 July (J. Wang et al. 2017), and the heat index, which was calculated by an algorithm from the U.S. National Weather Service (NWS; NWS 2011), reached 45.8°C, which was the highest level in 10 years. This article reports the use of observations to study the interactions between this heat wave and the UHI.

Observations from the AWS network; soil moisture sensors; ground-based remote sensing instruments such as a wind profiler, a ceilometer, and three radiometers in the SURF field campaign; and Global Forecast System final (FNL) gridded analysis data from the U.S. National Oceanic and Atmospheric Administration (NOAA) National Centers for Environmental Prediction (NCEP) are applied to provide a four-dimensional anatomy of the heat-wave event and to study the interactions between the UHI and the heat wave.

## 2. Data and study area

### a. Study area

Beijing, the capital of China, is one of the largest cities in the world. It is a directly controlled municipality that governs 16 urban, suburban, and rural districts. The city is located in the northern portion of the North China Plain, with the Yanshan and Taihang

Mountains bordering its north, northwest, and west. Most of the urban area is located on the plains in the south-central part of the city (Fig. 1a). The city has a typical monsoon-influenced (East Asian monsoon), semihumid and warm-temperate continental climate (Kottek et al. 2006) and hot and rainy summers.

Beijing was constructed on the concept of a ring-road (RR) system (shown by the red lines in Fig. 1a). The second–sixth RRs represent city expansion by urbanization. The second RR (innermost) traces the historic city core, which mostly consists of cultural relics and relatively low, old constructions. The second and fourth RRs constrain the central built-up area with denser and taller buildings. Between the fourth and sixth RRs are newly developed, less-dense urban areas as well as suburban areas. In this study, a rectangular study area was framed just outside the sixth RR (Fig. 1b).

### b. Data collection

#### 1) THE BEIJING AWS NETWORK

Approximately 300 AWSs exist in the Beijing metropolitan region. These AWSs were installed and implemented using the operational standards issued by the China Meteorological Administration (CMA 2003, 124–125) under the guidance of the World Meteorological Organization. All AWS data are under strict quality control by the methods described in Dou et al. (2008).

In this study, the hourly air temperature at 2 m, the relative humidity at 2 m, the pressure at 2 m, and the wind speed at 10 m from the AWSs were obtained from the Meteorological Information Center of the Beijing Meteorological Bureau.

Stations are selected if the percentage of missing reports of these four meteorological elements is less than 5% during the period of 8–15 July and if missing reports of temperature and wind are less than 35% during June–August (JJA) in the past decade from 2008 to 2017. The distribution of the 67 selected AWSs in the study area is shown in Fig. 1b. Because our study focuses on the urban area within the sixth RR, 51 stations inside the sixth RR were considered to be urban stations (red dots in Fig. 1b) (eight stations inside the sixth RR were excluded because they are located in large city parks, rural croplands or mountainous forests). In total, eight stations that are located outside of the urban zone were selected as rural reference stations (Fig. 1a) according to Yang et al. (2013) and Dou et al. (2015); all of the reference stations are situated on open ground in a countryside setting. The average elevation of the reference stations is 40.1 m, which is similar to the average elevation of the selected urban stations (45.6 m). Therefore, temperature corrections are not required for the elevation differences.

### 2) Ground-based remote sensors

Ground-based remote sensors—namely, three radiometers (Radiometrics Corporation MP-2000A) at Guanxiangtai (GXT), Haidian (HD), and Huairou (HR) stations; a wind profiler (China Aerospace Science and Industry Corp. CFL-03) at the HD station; and a ceilometer (Vaisala, Inc., CL51) at the HD station during the month of July 2017 from the SURF field campaign—were used to study the thermal profiles and vertical air movement during the heat-wave event. All of these sensors performed monitoring at high temporal resolutions, with values of 2 and 6 min and 16 s for the radiometers, wind profiler, and ceilometer, respectively. The GXT, HD, and HR stations have different surface conditions; specifically, GXT is a typical urban station surrounded by midrise buildings, HD is in a city park, and HR is a typical rural station surrounded by cropland. The locations of the three stations are shown in Fig. 1a. The differences in thermal conditions (virtual potential temperatures) in the boundary layer between

these three stations during heat-wave days and non-heat-wave days are analyzed. Non-heat-wave days refer to days outside the heat-wave period (9–13 July) in July 2017.

### 3) NCEP FNL analysis data

The NCEP FNL is a global spectral data assimilation and forecast model system giving 6-hourly (0000, 0600, 1200, and 1800 UTC) atmospheric variables at $1° \times 1°$ resolution and 26 levels (NOAA/NCEP 2000). The system collects observations from the Global Telecommunication System (GTS) and other sources. The 500-hPa geopotential heights field, 850-hPa specific humidity and wind field, and vertical wind field from NCEP FNL analysis data closest to the heat-wave event were applied to help investigate the synoptic causes of the heat-wave event.

### 4) Soil moisture and evaporation

Approximately 22 soil moisture stations exist within the Beijing metropolitan region, most of which are located outside the urban area. Hourly soil moisture observations in seven stations around the study area during July 2017 were obtained in this study (Fig. 1a). In addition, daily pan evaporation observations from GXT station were used to show the possible moisture source of this heat wave.

### c. Methods

### 1) Calculation of specific humidity and the heat index

Because this heat wave was accompanied by a relatively high near-surface atmospheric humidity content, the specific humidity and heat index are both considered in this study. Hourly values for air temperature, relative humidity, and pressure are used to calculate the specific humidity values following methods presented in Dai (2006).

The U.S. NWS algorithm (NWS 2011) performs well (Anderson et al. 2013) in reproducing the concept of apparent temperature (i.e., the heat index) proposed by Steadman (Steadman 1979a,b). The NWS algorithm contains a basic formula carried out by Rothfusz (1990) and allows several adjustments. In this study, we calculated the heat index following the NWS algorithm for each AWS per hour. The basic formula we used is shown below:

$$Hi = -42.379 + 2.049\,015\,23T + 10.143\,331\,27 \times RH - 0.224\,755\,41T \times RH - 0.006\,837\,83T^2$$
$$- 0.054\,817\,17 \times RH^2 + 0.001\,228\,74T^2 \times RH + 0.000\,852\,82T \times RH^2 - 0.000\,001\,99T^2 \times RH^2,$$

TABLE 1. Heatwave events over the past 10 years (2008–17) and rankings of the heat-wave events by different indices.

| Heatwave periods | Duration | | Max temperatures | | Max heat indices | |
|---|---|---|---|---|---|---|
| | Rankings | Values | Rankings | Values | Rankings | Values |
| 23–25 Jun 2009 | 3 | 3 days | 2 | 39.5°C | 8 | 37.0°C |
| 11–13 Aug 2009 | 3 | 3 days | 5 | 36.4°C | 5 | 39.3°C |
| 2–6 Jul 2010 | 1 | 5 days | 1 | 40.6°C | 7 | 38.1°C |
| 1–4 Jul 2012 | 2 | 4 days | 4 | 36.5°C | 2 | 40.8°C |
| 2–5 Jul 2013 | 2 | 4 days | 3 | 36.7°C | 4 | 39.6°C |
| 19–21 Jul 2014 | 3 | 3 days | 8 | 35.2°C | 3 | 40.6°C |
| 9–11 Jul 2016 | 3 | 3 days | 7 | 35.8°C | 6 | 39.1°C |
| 9–13 Jul 2017 | 1 | 5 days | 6 | 36.3°C | 1 | 45.8°C |

where Hi, $T$, and RH refer to heat index, temperature, and relative humidity, respectively.

### 2) HEAT-WAVE IDENTIFICATION

The methodological approach to define a heat wave is generally based on exceedance of a certain temperature threshold, either a relative threshold or an absolute threshold, for consecutive days (Meehl and Tebaldi 2004; Ding and Qian 2011). In this study, a heat wave is defined as a hot period lasting for at least three consecutive days with a maximum temperature exceeding 35°C (Liu et al. 2008). This definition is selected because it corresponds to the CMA heat warning and is consistent with many other studies focusing on heat-wave days in Beijing (Xie et al. 1999; Chen and Lu 2014; S. Jiang et al. 2019). Observations from the GXT station (39.8°N, 116.47°E) were selected to determine periods of heat wave because this station is the World Meteorological Organization station of Beijing and contains long-term, continuous, and representative observations. The absolute threshold of 35°C is at approximately the 91st percentile of the daily maximum temperature distribution with respect to the climatic period of 1988–2017 in JJA at GXT.

Heatwave event periods over the past 10 years (2008–17) were thus determined on the basis of observations from the GXT station and are listed in Table 1. Over the past 10 years, a total of eight heat-wave events occurred in Beijing. The duration, maximum temperature, and maximum heat index of each heat wave and the rankings of each heat wave among the total of eight heat waves by these three indices are shown in Table 1. The heat wave in 2017 is among the longest heat waves over the past 10 years. Although the temperature was not the highest among all heat-wave events, the calculated maximum heat index for this 2017 event ranked first with a value of 45.8°C (114.4°F), which was much higher than those of other heat waves.

### 3) CALCULATION OF UHI INTENSITY

UHI intensity (UHII) is generally expressed as the temperature difference between urban and rural areas.

UHII is estimated at every AWS to obtain the spatial pattern (P. Jiang et al. 2019). In this study, the UHII at a certain AWS is calculated as

$$\text{UHII}_i = T_i - T_{\text{rural}},$$

where $I = 1, 2, 3, \ldots$ denotes the $i$th station of the selected AWSs in the study area, $T_i$ is the 2-m air temperature for the $i$th station, and $T_{\text{rural}}$ is the average 2-m air temperature for the reference stations, which is defined as

$$T_{\text{rural}} = \frac{1}{n}\sum_{j=1}^{n} T_j,$$

where $j = 1, 2, 3, \ldots, n$, and $n$ is the number of reference stations.

The 67 selected AWSs in the study area are used to generate the UHII spatial patterns. This research focuses on the features of the canopy-layer UHI (2 m above ground) from in situ weather station observations; satellite-derived surface UHI data are beyond the scope of this paper. According to the CMA, the definition of one day is from 0800 local standard time (LST) on a given calendar day to 0800 LST on the next calendar day. In this research, daytime refers to 0800–2000 LST, and nighttime refers to 2000–0800 LST the next calendar day. Daytime and nighttime UHIs are thus calculated. The UHII during the heat wave was compared with the background, which is calculated by the mean UHII during 2008–17 in JJA.

## 3. Results

### a. Synoptic mechanisms of the heat-wave event

The circulation patterns and physical fields before (8 July), during (10 and 12 July) and after (14 July) the heat-wave event at 0800 LST are shown in Fig. 2. Before the heat wave, a precipitation event occurred during 6–8 July, with total of 41.7 mm of rainfall at GXT.
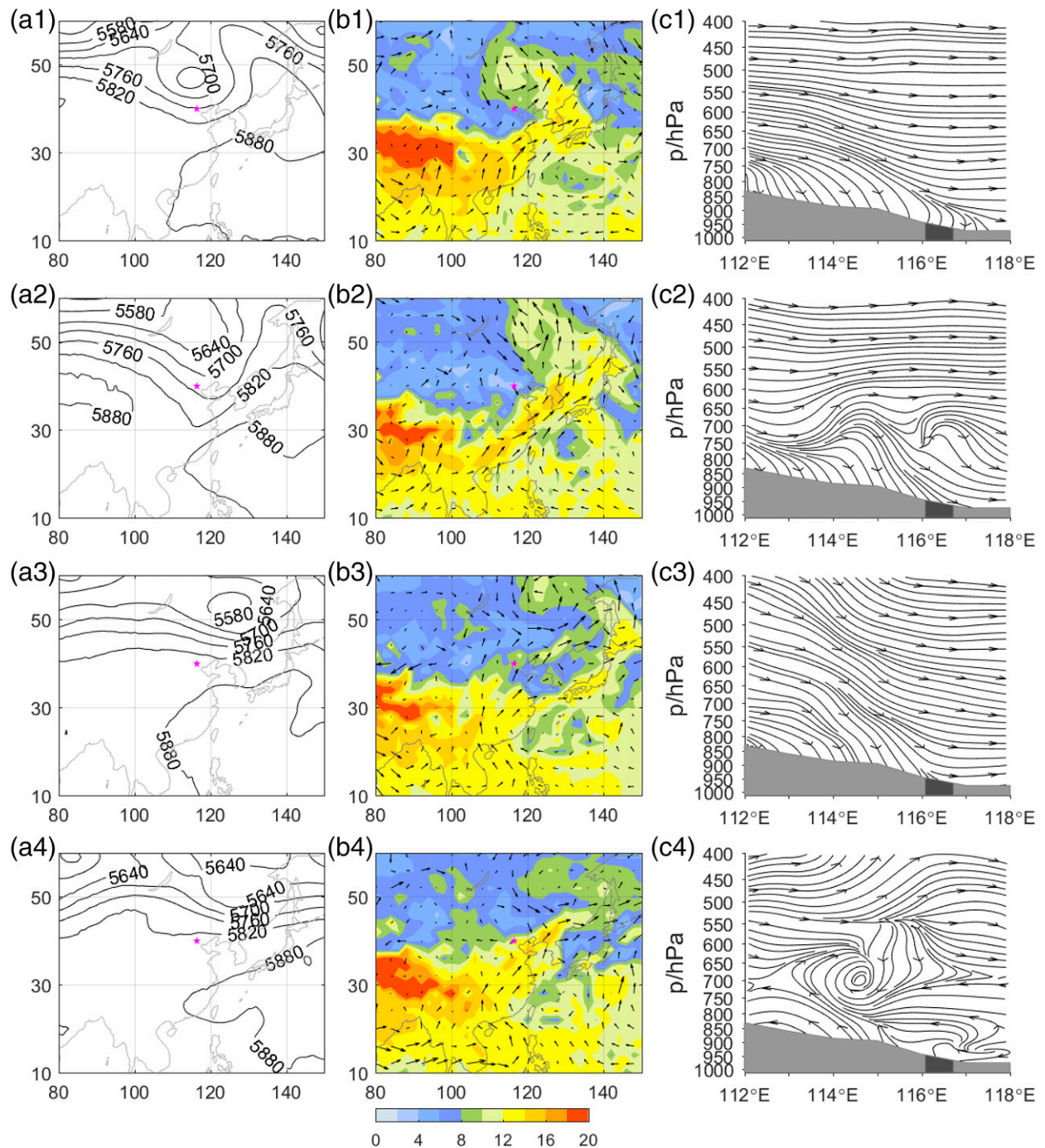
FIG. 2. Composites of the atmospheric field at 0800 LST (top) 8, (top middle) 10, (bottom middle) 12, and (bottom) 14 Jul for (a1)–(a4) the 500-hPa geopotential height (gpm; solid lines), (b1)–(b4) the 850-hPa specific humidity (k kg$^{-1}$; colors) and wind field (vectors), and (c1)–(c4) a cross section of the vertical wind field along 40°N from the NCEP FNL. The magenta points in (a1)–(a4) and (b1)–(b4) represent the study area. The dark-gray shading in (c1)–4(c4) represents the longitudinal scope of the study area.

Figure 2a(1) shows that on 8 July an extratropical cyclone developed in the north of Beijing. The 850-hPa specific humidity of the Beijing area was approximately 8–10 g kg$^{-1}$ [Fig. 2b(1)]. Westerly downslope winds

appeared along the 40°N cross section over Beijing [Fig. 2c(1)]. On 10 July, most of the East Asian continent was controlled by high pressure systems, and Beijing was located in the east of a high pressure ridge and in the
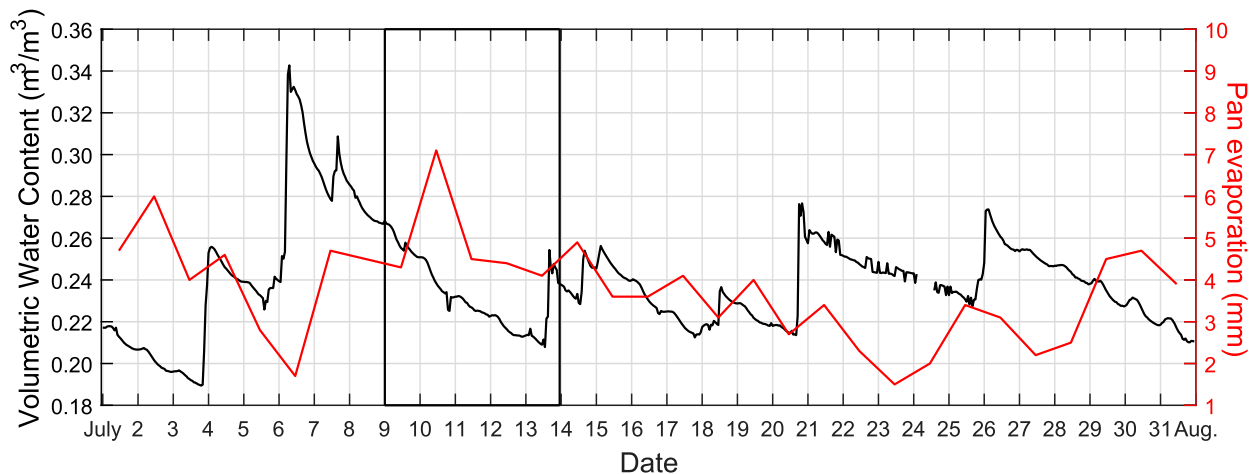
FIG. 3. Variabilities in the hourly mean volumetric water content ($m^3\,m^{-3}$) at 10 cm below ground level for seven soil moisture observation stations and the daily pan evaporation (mm) at the GXT station for July 2017. The period of the heat wave is denoted by the vertical black solid lines.

southwest of the cyclone [Fig. 2a(2)]. The 850-hPa specific humidity and wind field data revealed that Beijing was under relatively dry conditions (smaller than $4\,g\,kg^{-1}$) and northwest winds [Fig. 2b(2)]. At the 40°N cross section, Beijing was influenced by westward winds descending from the mountains [Fig. 2c(2)]. The circulation pattern on 10 July was a typical pattern for foehn-favorable heat waves on the North China Plain (Chen and Lu 2016). On 12 July, Beijing was under the control of the high pressure system [Fig. 2a(3)]. Southwest winds with relatively high specific humidity ($8$–$10\,g\,kg^{-1}$) occurred at the 850-hPa level [Fig. 2b(3)], which are not foehn favorable given that the mountains are located in the west/northwest/north side of the Beijing area. However, synoptic subsidence also induced descent over the Beijing area [Fig. 2c(3)]. Therefore, the high temperatures in Beijing were generally the result of dry adiabatic warming induced by the dynamic downslope and synoptic subsidence.

Precipitation events occurred at night on 13 and 14 July, which finally cooled the high temperatures. As shown in Fig. 2a(4), Beijing was located in a trough at 0800 LST 14 July. At the 850-hPa level, the specific humidity rose to above $12\,g\,kg^{-1}$, and northeast winds controlled the Beijing area [Fig. 2b(4)]. Easterly ascent appeared over Beijing [Fig. 2c(4)].

This heat wave has the highest heat index value among the eight heat waves in the past 10 years. The moisture sources of this heat waves were likely from both local evaporation and moisture advection. Figure 2b(3) shows that enhanced moisture ($8$–$10\,g\,kg^{-1}$) from the southwest was transported to Beijing area via southwesterly winds on 12 July. The time variations of soil moisture (indicated by the volumetric water content) and pan evaporation

during July 2017 are shown in Fig. 3. The pan evaporation can be used as a good indicator of evaporation when the land surface moisture supply is abundant (Brutsaert and Parlange 1998). The soil volumetric water content values were generally high (over $0.3\,m^3\,m^{-3}$) before the heat wave because precipitation occurred in Beijing on 6–8 July prior to the heat wave. Thus, the actual evaporation was likely not much less than the pan evaporation. The daily pan evaporation values were 4–7 mm during the heat wave, with the highest value occurring on 10 July (Fig. 3), when water vapor in the air was low. During the heat wave, soil moisture continued drying until the next precipitation event occurred on the night of 13 July. Therefore, local evaporation of the initial abundant soil moisture is another source of moisture for this heat wave. An additional possible source of moisture is anthropogenic latent heat due to the increased use of air conditioning systems in commercial buildings to mitigate the excessive heat and moisture.

## b. Vertical thermal structure and air movement

Figure 4 shows the vertical thermal structures, air movements, and boundary layer heights observed by ground-based remote sensors during the month of July 2017. All of the variables shown in Fig. 4 are based on a 3-h moving average of the raw data to reduce extreme values. Vertical air movements were observed by a wind profiler at HD station. As shown in Fig. 4, descending winds were dominant from 8 to 10 July, which is consistent with the synoptic background discussed in section 3a and showed that the dry adiabatic warming by the dynamic downslope and synoptic subsidence were the main causes of the heat-wave event. The strong ascent at night on 13 and 14 July corresponded to the
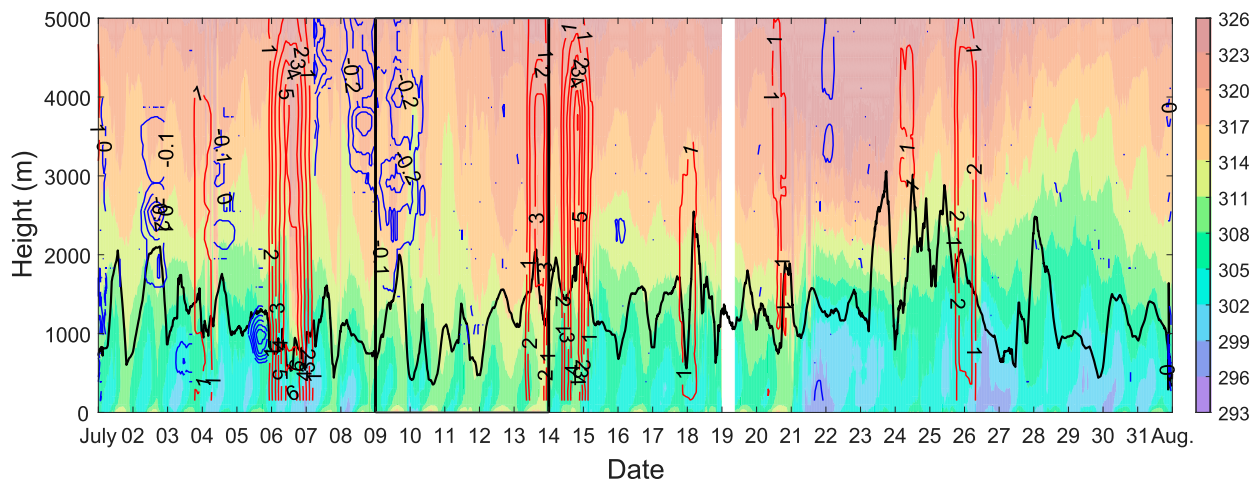
FIG. 4. The contours of the virtual potential temperature monitored by the radiometer (color-filled contour plot) at the GXT station, the contours of vertical wind speed (upward: red lines; downward: blue lines) determined by the wind profiler, and the PBL (black curve) determined by the ceilometer at the HD station. The period of the heat wave is denoted by the vertical black solid lines. The white bar indicates a period of missing data in the radiometer observations on 19 Jul.

precipitation events that occurred after the heat-wave event. Although subsidence also appeared on other non-heat-wave days, the scales and durations of these winds were not comparable with those of the winds on 8–10 July. The scale of the descent is nearly one order of magnitude smaller than that of the upward winds during precipitation (Fig. 4). Further, convective precipitation is common during the summer in Beijing and induces large, localized ascent.

The time series of the planetary boundary layer (PBL) height observed by the ceilometer at the HD station is also shown in Fig. 4. The mean PBL height during the heat-wave event was 1045 m, which was 291 m lower than that during non-heat-wave days (1336 m). The heat-wave PBL was lower than the PBL of non-heat-wave days, which may be related to this heat-wave event occurring in the middle of two precipitation events, with one occurring before the heat wave on 6–8 July and the other occurring after the heat wave starting on the night of 13–14 July. High air humidity and cloudy weather occurred during the last three days of the heat-wave event. This heat wave resembles the July 1999 heat wave in Chicago, Illinois, which also had a high apparent temperature, relatively higher soil moisture, and a shallow boundary layer (Kunkel et al. 1996).

The thermal structures of the atmosphere were continually monitored by the radiometer at GXT station (with only a short period of missing observations on 19 July). Figure 4 shows the contours of the virtual potential temperature from the ground to 5 km from 1 to 31 July. During the heat-wave event (9–13 July), the air near the surface was warmer (4.5 K higher within surface to 100 m) than that during non-heat-wave days in

July 2017. A superadiabatic layer near the surface could be observed in the daytime, which is similar to the findings of a recently reported study for the city of New York, New York (Ramamurthy et al. 2017). In general, the high pressure system created a thermal block and restrained the heat transfer between the PBL and the upper atmosphere. The heat and moisture released in the subsequent heat-wave days remained close to the surface and thereby worsened the conditions inside the boundary layer.

Figures 5a and 5b compare the profiles of the mean virtual potential temperature in stations with different surface conditions. This comparison shows that temperatures were highly elevated during the heat-wave period (9–13 July) compared to those during non-heat-wave days (1–8 and 14–18 July) at all three stations. Only data from 1 to 18 July were calculated because the radiometers stopped collecting observations on 19 July at the HR station. During the daytime, a superadiabatic layer occurred under 500 m and an elevated stable layer occurred above the GXT station, regardless of the heat-wave conditions (Fig. 4a). However, at the HD (urban park) station, the near-surface layers were stable during the daytime and nighttime while HR (rural) was neutral in the daytime and stable at nighttime. The difference between GXT and the other two stations may be due to different underlying surfaces as well as mountain breezes because the HR and HD stations are closer than GXT to the foot of the mountains. These results suggest that the thermal profiles within the boundary layer have a complex structure even within city areas, which is consistent with the findings of studies in other cities (Liu et al. 2006; Ramamurthy et al. 2017).
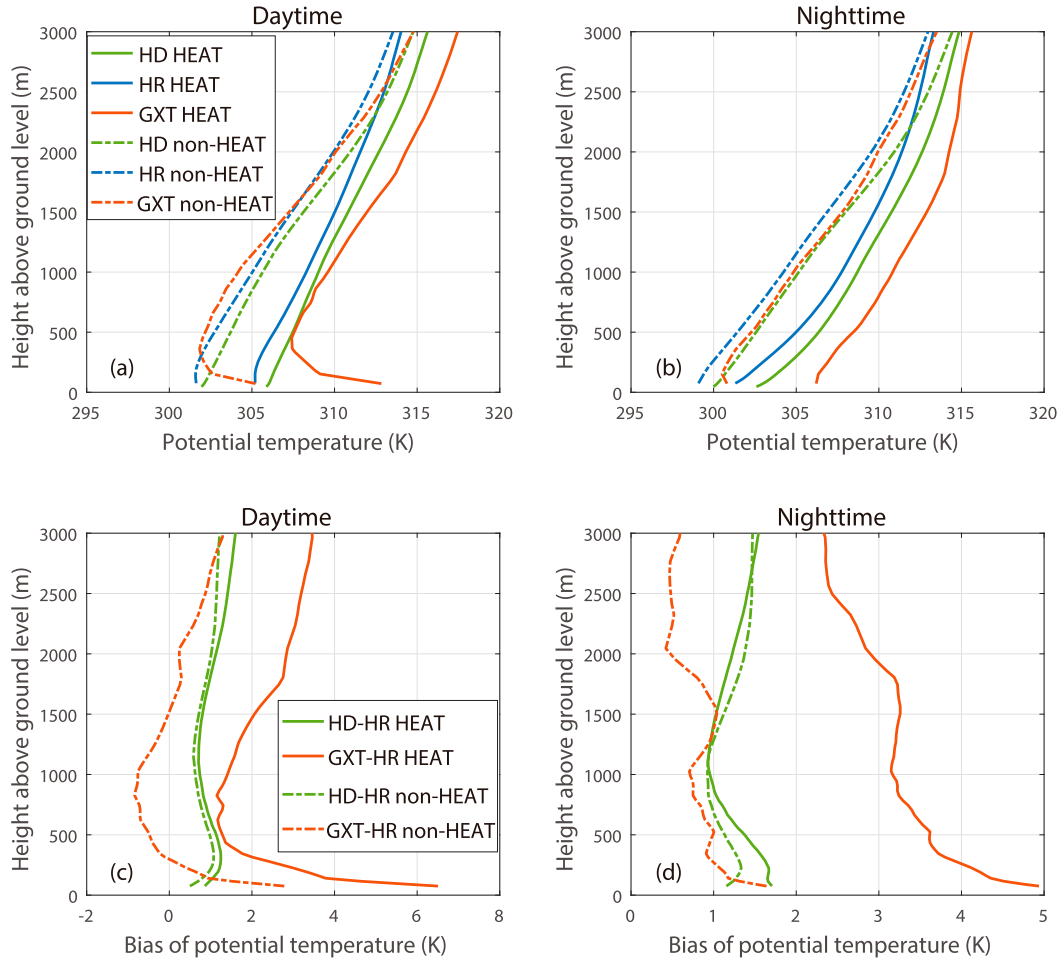
FIG. 5. (a),(b) The mean virtual potential temperature profiles at GXT (urban), HD (urban park), and HR (rural) and (c),(d) biases of the virtual potential temperature profiles between urban and rural stations during the heat-wave event (label "HEAT"; 9–13 Jul) and on non-heat-wave days (label "non-HEAT"; 1–8 and 14–18 Jul) in the (left) daytime (0800–1900 LST) and (right) at night (2000–0700 LST).

The results of subtracting the virtual potential temperature profiles at HR (rural) from those in GXT and HD (urban) are shown in Figs. 5c and 5d. The two urban stations generally had higher virtual potential temperatures than the HR station, illustrating that the impact of the canopy heat island extended to the overlying atmosphere. The virtual potential temperatures at GXT station were smaller than those at HR station during non-heat-wave days in the 300–1500-m layer in the daytime, which may be related to the decline in the virtual potential temperature with height caused by the superadiabatic layer at GXT station and the less energized urban boundary layer during non-heat-wave days as compared with heat-wave days. The differences in the thermal conditions within boundary layers between GXT and HR were much greater during heat-wave days than those during non-heat-wave days (on average, 2.4 K greater during the daytime and 2.9 K greater during the

nighttime from the surface to 3000 m). The difference between the HD and HR thermal conditions on heat-wave days and non-heat-wave days increased slightly (on average, 0.4 K larger during the daytime and 0.3 K larger during the nighttime from the surface to 3000 m) and was smaller than that of non-heat-wave days during the nighttime above 1100 m. Li et al. (2016) showed that the positive interaction between UHIs and heat waves not only exists at the surface but also in higher levels (up to 70 m). Results of our study suggest that the positive interaction between UHIs and HWs persist to nearly the entire boundary layer.

### c. Processes and features of the heat-wave event

The time series of temperatures, heat index values, and daily maximum power loads from 9 to 15 July are shown in Fig. 6a. The mean daytime maximum temperatures of the 51 urban stations in 6 RRs and the rural stations showed the highest values during the early
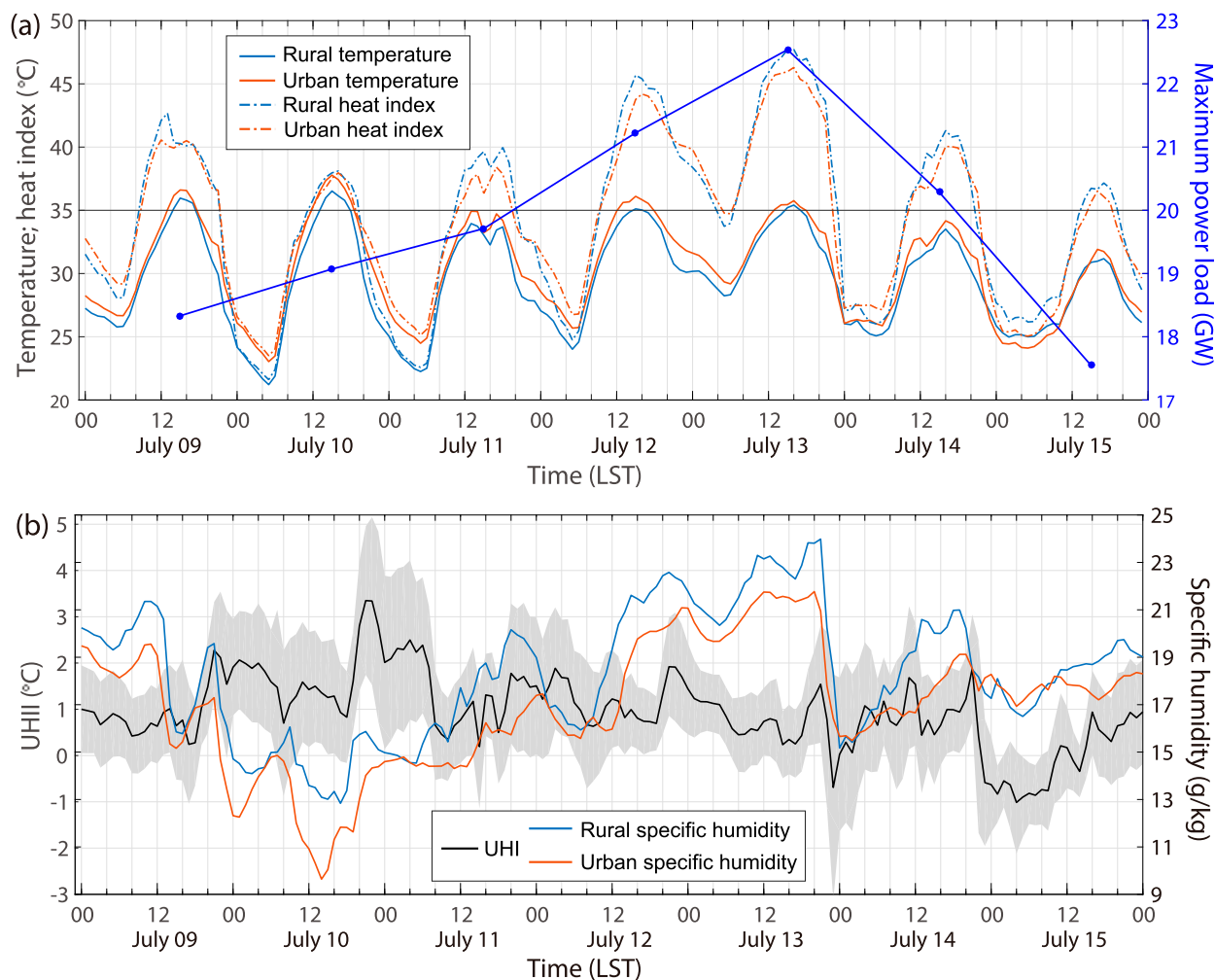
FIG. 6. (a) Time series of the mean rural and urban temperatures (solid lines) and heat indices (dash–dotted lines) at stations from 9 to 15 Jul. The daily maximum electric power loads from 9 to 15 Jul are shown by blue lines, with blue dots representing the values. (b) Time series of the mean UHIIs (gray shading designate the standard deviation of the value for the 51 urban stations) and the mean rural and urban specific humidity from 9 to 15 Jul. Variables for urban areas were calculated from the 51 stations within the six RRs, and variables for rural areas were calculated from the eight selected reference stations.

afternoon of 10 July. However, the nighttime minimum temperatures of the rural stations and urban stations both continued increasing after 9 July and reached the highest values on the early morning of 13 July. From 11 to 13 July, urban nighttime temperatures remained constant above 25°C. The daytime and nighttime heat index values during the heat-wave event both increased from 10 to 13 July. The temperature and heat index values during the night of 12 July in urban areas were generally higher than 28° and 34°C, respectively. Such high temperature and high heat index during nighttime could lead to insufficient recovery from the thermal stress experienced during daytime.

Time series of the UHIIs from 9 to 15 July are shown in Fig. 6b. The UHII was much higher during the nighttime on 10 July (from 2000 LST 10 July to 0800 LST 11 July) than that during nighttime on other days. The highest UHIIs were 8.05°C at an urban station inside the second RR at 2300 LST and 3.35°C for the average of the 51 urban stations in the sixth RR at 2100 LST 10 July. On 10 July, few clouds were observed, and specific humidity near the surface (Fig. 6b) and at the 850-hPa level (Fig. 2) were the lowest during the period of the heat-wave event. According to previous studies (Hardin et al. 2018; Eastin et al. 2018), UHII is generally higher under clear-sky and low vapor conditions. Figure 6b shows that the specific humidity in rural and urban areas continued rising from 10 to 13 July. In the days after 10 July, as the air humidity rose and clouds formed, the differences in temperature between urban and rural areas shrank.
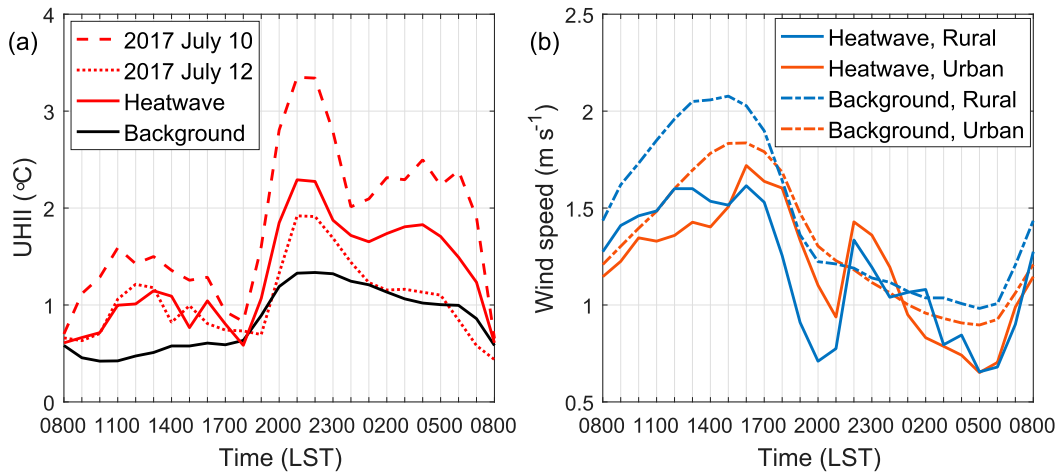
FIG. 7. (a) Diurnal cycles of the mean UHIIs within the six RRs during the heat wave in 2017 (red lines) and the mean UHII for the background during 2008–17 in JJA (black line). Diurnal cycles of 10 (dashed line) and 12 (dotted line) Jul in the heat wave are separately plotted. (b) Diurnal cycles of the mean rural and urban wind speeds during the heat wave (solid lines) and for the background during 2008–17 in JJA (dash–dotted lines).

The standard deviations of the UHIIs for the 51 urban stations are shown as the gray shading area in Fig. 6b, which were highest on 10 July (1.45°C) and lowest on 12 July (0.87°C). The standard deviations of the temperatures for the rural stations show variations that are similar to those of the UHIIs for the urban stations, but they have generally smaller values (not shown).

Except on 10 July, the heat index values in rural areas during the daytime were higher than those in urban areas (Fig. 6a). On 13 July, the heat index was extraordinarily high, with a mean value of 47.8°C for the 8 rural stations at 1600 LST 13 July, which was slightly higher than the mean heat index in urban areas (46.3°C) at the same time. Figure 6b shows that the specific humidity was generally higher in rural areas than urban areas throughout the heat-wave events, suggesting that under high-temperature and high-humidity conditions, the heat index values in rural areas can be higher than those in urban areas due to the reduced urban humidity. However, at nighttime when the UHI effect was strong, the heat index was higher in urban zones than that in rural areas.

The daily maximum electric power load in Beijing increased from 9 July (Sunday) to 13 July (Thursday) and then decreased distinctly (Fig. 6a). This pattern differs from the average summertime weekly cycle of daily maximum electric power load in Beijing, which presents small variations with the values slightly higher in weekdays (about 1 GW) than in weekends. The changes in the daily maximum electric power load were more consistent with the time variations in the heat index than with temperatures (except on 9 July, just after the precipitation event on 6–8 July). This indicates that the heat index influences more than the temperature on

human activities during heat waves for the case of Beijing. The maximum electric power demand reached a peak of 22.54 GW on 13 July, which coincided with the maximum heat index. A high heat index represents high temperatures and humidity, which trigger building energy demands for cooling and dehumidification (Ortiz et al. 2018a). This event also demonstrates the vulnerability of the electrical infrastructure in large cities to intense heat events.

### d. Characteristics of enhanced UHII

Figure 7a shows that two peaks occurred in the diurnal cycles of UHIIs during the heat wave, with one weak peak occurring at approximately 1400 LST in the early afternoon and one strong peak occurring at night, which is similar to the diurnal cycles of UHII during heat waves in Beijing in a recent study by S. Jiang et al. (2019). Both daytime and nighttime UHII were enhanced during the heat wave relative to the background decadal mean. The mean UHII diurnal cycle during JJA over the past 10 years was similar to the results of analyses of diurnal cycles of typical summers in Beijing (K. Wang et al. 2017, their Fig. 8), with only one noticeable peak during the nighttime. During the heat-wave event, the diurnal cycles of UHII demonstrate a second peak during the day (Fig. 7a), which corresponds to the obvious double peak of diurnal cycles caused by cooling loads from buildings in Beijing during heat waves as recently reported by Xu et al. (2018, their Fig. 5). This result indicates that anthropogenic heat plays an important role in the UHI during the heat-wave event in Beijing.

Wind speed is a factor that may influence the temperatures and UHIs. Diurnal cycles of wind speed in
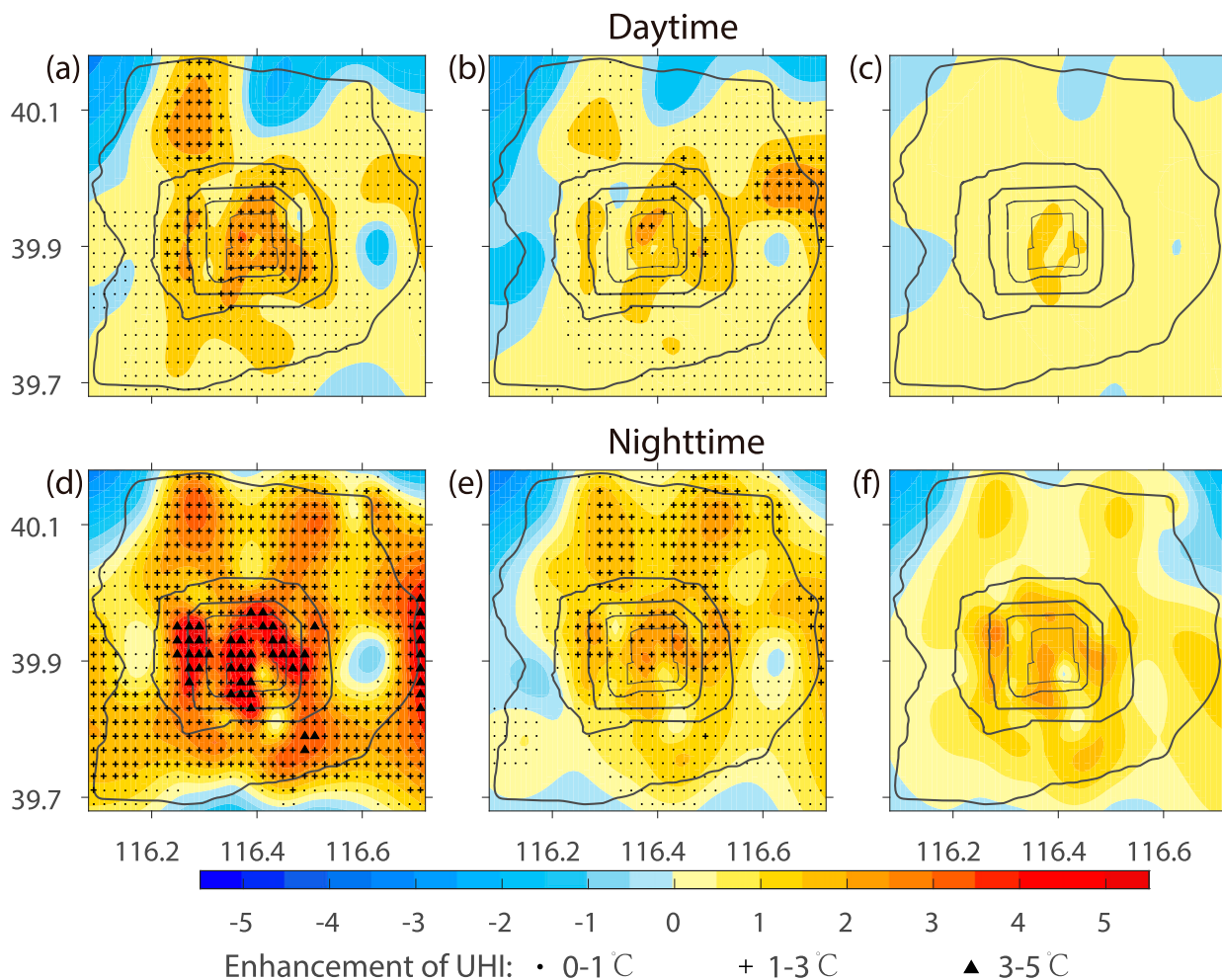
FIG. 8. The mean UHII in the study area for (a) daytime 0800–1900 LST 10 Jul 2017, (b) daytime 0800–1900 LST 12 Jul 2017, (c) daytime background of the decadal average during JJA, (d) nighttime from 2000 LST 10 Jul to 0700 LST 11 Jul 2017, (e) nighttime from 2000 LST 12 to 0700 LST 13 Jul 2017, and (f) nighttime background of the decadal average during JJA. The symbols in (a), (b), (d), and (e) indicate the areas in which the UHII was larger during the heat wave than it was over the background period, with different symbols indicating different degrees of enhanced UHII during the heat wave. Black lines show the second, third, fourth, fifth, and sixth RR from inner to outer.

urban and rural areas during the heat wave and against the background of decadal mean are shown in Fig. 7b. Wind speed during the heat wave was generally lower than the background except around 2300 LST in the nighttime. After verifying the wind speed day by day, we found that the enhanced wind speed occurred in the night of 9–10 July; a possible reason may be that the sky was clear and nighttime radiative cooling was stronger at the beginning of this heat wave, thus inducing higher mountain breezes at night. According to Li et al. (2016), increased wind speed during the nighttime strengthens the advective cooling and thus weakens the UHII. Figure 7a shows that the UHII dropped after 2200 during the heat wave and then increased at 0100, which may be related to the enhanced wind speed in the period of 2200–0100 (Fig. 7b). Contrary to nighttime wind speed,

increases of daytime urban wind speed amplify the UHII because of a stronger sensible effect (Li et al. 2016). During the heat wave, enhanced daytime urban wind speed compared to rural wind speed was not obvious on 9 July but was obvious on 10–13 July (not shown), suggesting that the heat island transitioned into a heat plume in the daytime of 10–13 July.

Water vapor is also a synergistic factor between UHIs and heat waves. As shown in Fig. 2 and Fig. 6b, 10 July was under the driest condition and 12 July was under the most humid condition (13 July is not considered because the nighttime specific humidity dropped when precipitation occurred). Therefore, the diurnal cycles and spatial distributions of UHIIs for 10 and 12 July were separately plotted in Fig. 7a and Fig. 8. Figure 7a shows that both 10 and 12 July have shown amplified UHII

relative to the background. However, the UHIIs were much higher on 10 July than on 12 July. Lower water vapor in the atmosphere and less cloudy conditions allow for the urban areas to receive more solar radiation while the rural areas tend to cool faster through nighttime radiative cooling, therefore UHIIs were much higher on 10 July. The reason that the UHIIs on 12 July were still enhanced relative to the background may be the strong anthropogenic heating, indicated by the daily maximum electric power load (Fig. 6a), and the positive effect of wind speed on the interaction between the UHII and the heat wave. Figures 8a and 8d show that both the daytime and nighttime UHIIs were enhanced (areas with symbols) in most of the urban areas relative to the backgrounds on 10 July. On 12 July, there are some urban areas in which UHIIs were not enhanced, which are mainly located in the west areas close to the mountains between the fifth and sixth RRs. These results indicate that cloud and water vapor conditions play an important role in influencing the interaction between UHIs and heat waves. Some less-dense urban areas can experience reduced UHII during heat waves compared to the background when the water vapor is high.

The spatial pattern of daytime UHIIs during this heat-wave event (Figs. 8a,b) was similar to the decadal average pattern (Fig. 8c), and the same result was observed at night (Figs. 8d–f). However, the spatial patterns of daytime UHIIs differ from the spatial patterns of nighttime UHIIs. The daytime UHIIs on 10 and 12 July were generally higher in the city center, in the northwest area between the fifth and sixth RRs, and around the sixth RRs in the east. The UHII patterns during the nighttime had a different multicenter distribution than those during the daytime. At night, the UHIIs were highest around the city center. They were also high in the northwest, northeast, and southeast between the fifth and sixth RRs and around the sixth RRs in the east (Figs. 8d–f). The differences between the daytime and nighttime spatial patterns of UHIIs may be due to the different factors affecting the UHI. During daytime, anthropogenic heat emissions and contrast water availability between urban and rural areas control the UHIIs. During nighttime, release of stored heat controls the UHIIs so that the spatial pattern of nighttime UHII shows dependence on the morphological aspects of the city (Oke 1982; Ramamurthy et al. 2014).

## 4. Discussion and conclusions

The focus of this study is an analysis of an intense heat episode interacting with a strong UHI during 9–13 July 2017 that took place in Beijing that had high impacts on natural and human variables, including record-setting daily electricity consumption and historically high heat index records. A suite of local and mesoscale instruments situated in and around the city were used to analyze the causation of the heat wave and the role that Beijing urbanization played in this heat-wave event.

This heat-wave event has both high-temperature and high-humidity characteristics. At the beginning of the heat wave, dynamic downslope and synoptic subsidence induced dry adiabatic warming, which increased the surface temperatures. In the following days, the surface moisture increased from both local evaporation and moisture advection. The high pressure system over the Beijing area suppressed the surface heat and moisture inside the boundary layer. As the atmospheric circulation changed, with the high moisture in the air and the induction of convective heat, precipitation occurred, which finally reduced the high temperatures. This heat wave has many similar characteristics with the July 1999 heat wave in Chicago (Kunkel et al. 1996), including initial abundant soil moisture, decreased boundary layer, and high apparent temperature, which contrast from some other studies and events with soil desiccation and deeper convective boundary layer in the heat waves (Miralles et al. 2014; Ramamurthy and Bou-Zeid 2017).

This heat-wave event reflected the evolution of the impacts of urbanization on the local climate. The interactions between the UHI and the heat wave can be summarized via the following six points.

1) Not only were the mean canopy-layer UHIIs enhanced during the heat wave, but also the differences in thermal conditions between urban and rural throughout the entire boundary layer were enhanced during the heat wave.
2) Complex thermal structures exist even within the scope of the city according to the different underlying surfaces. The urban station (GXT) observed a lifted stable layer above a superadiabatic layer during the day, whereas the urban park station (HD) observed stable layers in the near-surface air during the day.
3) A special pattern of diurnal UHII cycle was observed in the heat wave. The diurnal cycle of the decadal average UHII in summer presents one peak in the early nighttime. During the heat-wave event, the diurnal cycle generally has two peaks, with one weak peak in the daytime and one stronger peak in the nighttime. This pattern of diurnal UHII cycle during heat waves in Beijing was also observed in S. Jiang et al. (2019).
4) The UHII is generally higher inside the city center, consistent with the spatial pattern of UHII presented in Yang et al. (2013). Because different factors

(i.e., anthropogenic heat release, water availability, and modification of the land surface) control the diurnal cycle of UHIIs, the UHII spatial patterns showed different multicenter distributions for daytime and nighttime.

5) Water vapor and wind speed conditions influenced the interaction between the UHII and the heat wave. Even within the same heat-wave event, UHIIs presented large variabilities with respect to the changes of water vapor and wind speed. Some less-dense urban areas near the mountain have shown reduced UHII relative to background when the air humidity was high during the heat wave.

6) The urban area was more impacted by heat waves at nighttime. Because urban areas are generally drier than surrounding rural areas, heat index values tend to be higher in rural areas than those in urban areas during the day. However, due to the strong UHI effect, the heat index values were sustained at higher levels in urban areas at night compared with those in rural areas. This result is consistent with Fischer et al.'s (2012) finding that urban humidity deficit only weakly counteracts the enhanced heat stress due to the large nighttime UHII.

Although this research used multiple sources of observations and analyzed the three-dimensional UHI characteristics under a heat-wave event, this investigation had shortcomings that were mainly associated with the focus on only one case study. Our results suggest that the heat index may be a better predictor variable for the daily maximum electric power load in summer than the temperature, but a more accurate relationship should be established. Moreover, the effect of anthropogenic heat release on the diurnal cycle of UHIIs also needs to be investigated. These shortcomings necessitate further research on the genesis and impacts of heat waves using observations and numerical studies.

REFERENCES

Ackerman, S. A., and J. Knox, 2012: *Meteorology: Understanding the Atmosphere.* 3rd ed. Jones and Bartlett Learning, 578 pp.

Anderson, G. B., M. L. Bell, and R. D. Peng, 2013: Methods to calculate the heat index as an exposure metric in environmental health research. *Environ. Health Perspect.*, **121**, 1111–1119, https://doi.org/10.1289/ehp.1206273.

Ao, X., L. Wang, X. Zhi, W. Gu, H. Yang, and D. Li, 2019: Observed synergies between urban heat islands and heat waves and their controlling factors in Shanghai, China. *J. Appl. Meteor. Climatol.*, **58**, 1955–1972, https://doi.org/10.1175/JAMC-D-19-0073.1.

Basara, J. B., H. G. Basara, B. G. Illston, and K. C. Crawford, 2010: The impact of the urban heat island during an intense heat wave in Oklahoma City. *Adv. Meteor.*, **2010**, 230365, https://doi.org/10.1155/2010/230365.

Braga, A. L. F., A. Zanobetti, and J. Schwartz, 2002: The effect of weather on respiratory and cardiovascular deaths in 12 U.S. cities. *Environ. Health Perspect.*, **110**, 859–863, https://doi.org/10.1289/ehp.02110859.

Brutsaert, W., and M. B. Parlange, 1998: Hydrologic cycle explains the evaporation paradox. *Nature*, **396**, 30, https://doi.org/10.1038/23845.

Chen, R., and R. Lu, 2014: Dry tropical nights and wet extreme heat in Beijing: Atypical configurations between high temperature and humidity. *Mon. Wea. Rev.*, **142**, 1792–1802, https://doi.org/10.1175/MWR-D-13-00289.1.

——, and ——, 2016: Role of large-scale circulation and terrain in causing extreme heat in western North China. *J. Climate*, **29**, 2511–2527, https://doi.org/10.1175/JCLI-D-15-0254.1.

Chen, T., 2017: Time-series analysis of heat waves and emergency department visits in Atlanta, 1993 to 2012. *Environ. Health Perspect.*, **125**, 057009, https://doi.org/10.1289/EHP44.

Ciais, P., and Coauthors, 2005: Europe-wide reduction in primary productivity caused by the heat and drought in 2003. *Nature*, **437**, 529–533, https://doi.org/10.1038/nature03972.

Clark, E. C., R. D. Bornstein, and Y. T. Tam, 1985: Current and potential anthropogenic moisture effects on the New York City planetary boundary layer. *J. Air Pollut. Control Assoc.*, **35**, 831–835, https://doi.org/10.1080/00022470.1985.10465963.

CMA, 2003: *Specification of Ground Meteorological Observation* (in Chinese). China Meteorological Press, 151 pp.

Cristo, R. D., A. Mazzarella, and R. Viola, 2007: An analysis of heat index over Naples (southern Italy) in the context of European heat wave of 2003. *Nat. Hazards*, **40**, 373–379, https://doi.org/10.1007/s11069-006-0033-7.

Dai, A., 2006: Recent climatology, variability, and trends in global surface humidity. *J. Climate*, **19**, 3589–3606, https://doi.org/10.1175/JCLI3816.1.

Daniel, M., A. Lemonsu, and V. Viguié, 2018: Role of watering practices in large-scale urban planning strategies to face the heat-wave risk in future climate. *Urban Climate*, **23**, 287–308, https://doi.org/10.1016/j.uclim.2016.11.001.

Davis, R. E., D. M. Hondula, and A. P. Patel, 2016: Temperature observation time and type influence estimates of heat-related mortality in seven U.S. cities. *Environ. Health Perspect.*, **124**, 795–804, https://doi.org/10.1289/ehp.1509946.

Ding, T., and W. Qian, 2011: Geographical patterns and temporal variations of regional dry and wet heatwave events in China during 1960–2008. *Adv. Atmos. Sci.*, **28**, 322–337, https://doi.org/10.1007/s00376-010-9236-7.

Dou, J., Y. Wang, R. Bornstein, and S. Miao, 2015: Observed spatial characteristics of Beijing urban climate impacts on summer thunderstorms. *J. Appl. Meteor. Climatol.*, **54**, 94–105, https://doi.org/10.1175/JAMC-D-13-0355.1.

Dou, Y., Y. Qu, S. Tao, and B. Hu, 2008: The application of quality control procedures for real time data from automatic weather stations (in Chinese). *Meteor. Mon.*, **34**, 77–81, https://doi.org/10.7519/j.issn.1000-0526.2008.08.012.

Eastin, M. D., M. Baber, A. Boucher, S. Di Bari, R. Hubler, B. Stimac-Spalding, and T. Winesett, 2018: Temporal variability of the

Charlotte (sub)urban heat island. *J. Appl. Meteor. Climatol.*, **57**, 81–102, https://doi.org/10.1175/JAMC-D-17-0099.1.

Fischer, E. M., K. W. Oleson, and D. M. Lawrence, 2012: Contrasting urban and rural heat stress responses to climate change. *Geophys. Res. Lett.*, **39**, L03705, https://doi.org/10.1029/2011GL050576.

Founda, D., and M. Santamouris, 2017: Synergies between urban heat island and heat waves in Athens (Greece), during an extremely hot summer (2012). *Sci. Rep.*, **7**, 10973, https://doi.org/10.1038/s41598-017-11407-6.

González, J. E., and Coauthors, 2019: New York City panel on climate change 2019 report chapter 2: New methods for assessing extreme temperatures, heavy downpours, and drought. *Ann. N. Y. Acad. Sci.*, **1439**, 30–70, https://doi.org/10.1111/nyas.14007.

Hardin, A. W., Y. Liu, G. Cao, and J. K. Vanos, 2018: Urban heat island intensity and spatial variability by synoptic weather type in the northeast U.S. *Urban Climate*, **24**, 747–762, https://doi.org/10.1016/j.uclim.2017.09.001.

Iamarino, M., S. Beevers, and C. S. B. Grimmond, 2012: High-resolution (space, time) anthropogenic heat emissions: London 1970–2025. *Int. J. Climatol.*, **32**, 1754–1767, https://doi.org/10.1002/joc.2390.

Jacobson, M. Z., S. V. Nghiem, A. Sorichetta, and N. Whitney, 2015: Ring of impact from the mega-urbanization of Beijing between 2000 and 2009. *J. Geophys. Res. Atmos.*, **120**, 5740–5756, https://doi.org/10.1002/2014JD023008.

Jiang, P., X. Liu, H. Zhu, and Y. Li, 2019: Features of urban heat island in mountainous Chongqing from a dense surface monitoring network. *Atmosphere*, **10**, 67, https://doi.org/10.3390/atmos10020067.

Jiang, S., X. Lee, J. Wang, and K. Wang, 2019: Amplified urban heat islands during heat wave periods. *J. Geophys. Res. Atmos.*, **124**, 7797–7812, https://doi.org/10.1029/2018JD030230.

Karl, T. R., and R. W. Knight, 1997: The 1995 Chicago heat wave: How likely is a recurrence? *Bull. Amer. Meteor. Soc.*, **78**, 1107–1119, https://doi.org/10.1175/1520-0477(1997)078<1107:TCHWHL>2.0.CO;2.

Kottek, M., J. Grieser, C. Beck, B. Rudolf, and F. Rubel, 2006: World map of the Köppen-Geiger climate classification updated. *Meteor. Z.*, **15**, 259–263, https://doi.org/10.1127/0941-2948/2006/0130.

Kunkel, K. E., S. A. Changnon, B. C. Reinke, and R. W. Arritt, 1996: The July 1995 heat wave in the Midwest: A climatic perspective and critical weather factors. *Bull. Amer. Meteor. Soc.*, **77**, 1507–1518, https://doi.org/10.1175/1520-0477(1996)077<1507:TJHWIT>2.0.CO;2.

Li, D., and E. Bou-Zeid, 2013: Synergistic interactions between urban heat islands and heat waves: The impact in cities is larger than the sum of its parts. *J. Appl. Meteor. Climatol.*, **52**, 2051–2064, https://doi.org/10.1175/JAMC-D-13-02.1.

——, T. Sun, M. Liu, L. Yang, L. Wang, and Z. Gao, 2015: Contrasting responses of urban and rural surface energy budgets to heat waves explain synergies between urban heat islands and heat waves. *Environ. Res. Lett.*, **10**, 054009, https://doi.org/10.1088/1748-9326/10/5/054009.

——, ——, ——, L. Wang, and Z. Gao, 2016: Changes in wind speed under heat waves enhance urban heat islands in the Beijing metropolitan area. *J. Appl. Meteor. Climatol.*, **55**, 2369–2375, https://doi.org/10.1175/JAMC-D-16-0102.1.

Liang, X., and Coauthors, 2018: SURF: Understanding and predicting urban convection and haze. *Bull. Amer. Meteor. Soc.*, **99**, 1391–1413, https://doi.org/10.1175/BAMS-D-16-0178.1.

Liu, L., L. Sun, Y. Liao, Y. Zhu, X. Zou, Y. Wang, and J. Yan, 2008: Development and application of national prediction system

for extreme high temperature (in Chinese). *Meteor. Mon.*, **34**, 103–107, https://doi.org/10.7519/j.issn.1000-0526.2008.10.014.

Liu, Y., F. Chen, T. Warner, and J. B. Basara, 2006: Verification of a mesoscale data-assimilation and forecasting system for the Oklahoma City area during the Joint Urban 2003 field project. *J. Appl. Meteor. Climatol.*, **45**, 912–929, https://doi.org/10.1175/JAM2383.1.

Meehl, G. A., and C. Tebaldi, 2004: More intense, more frequent, and longer lasting heat waves in the 21st century. *Science*, **305**, 994–997, https://doi.org/10.1126/science.1098704.

Miao, S., F. Chen, M. A. Lemone, M. Tewari, Q. Li, and Y. Wang, 2009: An observational and modeling study of characteristics of urban heat island and boundary layer structures in Beijing. *J. Appl. Meteor. Climatol.*, **48**, 484–501, https://doi.org/10.1175/2008JAMC1909.1.

Miralles, D. G., A. J. Teuling, C. C. van Heerwaarden, and J. V.-G. de Arellano, 2014: Mega-heatwave temperatures due to combined soil desiccation and atmospheric heat accumulation. *Nat. Geosci.*, **7**, 345–349, https://doi.org/10.1038/ngeo2141.

Morris, C. J. G., I. Simmonds, and N. Plummer, 2001: Quantification of the influences of wind and cloud on the nocturnal urban heat island of a large city. *J. Appl. Meteor.*, **40**, 169–182, https://doi.org/10.1175/1520-0450(2001)040<0169:QOTIOW>2.0.CO;2.

NOAA/NCEP, 2000: NCEP FNL Operational Model Global Tropospheric Analyses, continuing from July 1999 (updated daily). National Center for Atmospheric Research Computational and Information Systems Laboratory Research Data Archive, accessed 10 October 2017, https://doi.org/10.5065/D6M043C6.

NWS, 2011: Meteorological conversions and calculations: Heat index calculator. NOAA, https://www.wpc.ncep.noaa.gov/html/heatindex.shtml.

Oke, T. R., 1982: The energetic basis of the urban heat island. *Quart. J. Roy. Meteor. Soc.*, **108**, 1–24, https://doi.org/10.1002/qj.49710845502.

Ortiz, L. E., J. E. Gonzalez, and W. Lin, 2018a: Climate change impacts on peak building cooling energy demand in a coastal megacity. *Environ. Res. Lett.*, **13**, 094008, https://doi.org/10.1088/1748-9326/aad8d0.

——, ——, W. Wu, M. Schoonen, J. Tongue, and R. Bornstein, 2018b: New York City impacts on a regional heat wave. *J. Appl. Meteor. Climatol.*, **57**, 837–851, https://doi.org/10.1175/JAMC-D-17-0125.1.

Parente, J., M. G. Pereira, M. Amraoui, and E. M. Fischer, 2018: Heat waves in Portugal: Current regime, changes in future climate and impacts on extreme wildfires. *Sci. Total Environ.*, **631–632**, 534–549, https://doi.org/10.1016/j.scitotenv.2018.03.044.

Patz, J. A., D. Campbell-Lendrum, T. Holloway, and J. A. Foley, 2005: Impact of regional climate change on human health. *Nature*, **438**, 310–317, https://doi.org/10.1038/nature04188.

Ramamurthy, P., and E. Bou-Zeid, 2017: Heatwaves and urban heat islands: A comparative analysis of multiple cities. *J. Geophys. Res. Atmos.*, **122**, 168–178, https://doi.org/10.1002/2016JD025357.

——, ——, Z. Wang, M. Baeck, J. Smith, J. Hom, and N. Saliendra, 2014: Influence of subfacet heterogeneity and material properties on the urban surface energy budget. *J. Appl. Meteor. Climatol.*, **53**, 2114–2129, https://doi.org/10.1175/JAMC-D-13-0286.1.

——, J. González, L. Ortiz, M. Arend, and F. Moshary, 2017: Impact of heatwave on a megacity: An observational analysis of New York City during July 2016. *Environ. Res. Lett.*, **12**, 054011, https://doi.org/10.1088/1748-9326/aa6e59.

Rizvi, S. H., K. Alam, and M. J. Iqbal, 2019: Spatio-temporal variations in urban heat island and its interaction with heat wave. *J. Atmos. Sol.-Terr. Phys.*, **185**, 50–57, https://doi.org/10.1016/j.jastp.2019.02.001.

Rothfusz, L. P., 1990: The heat index "equation" (or, more than you ever wanted to know about heat index). National Weather Service Tech. Attachment 90-23, 2 pp., https://www.weather.gov/media/ffc/ta_htindx.PDF.

Scott, A. A., D. W. Waugh, and B. Zaitchik, 2018: Reduced urban heat island intensity under warmer conditions. *Environ. Res. Lett.*, **13**, 064003, https://doi.org/10.1088/1748-9326/aabd6c.

Sherwood, S. C., and M. Huber, 2010: An adaptability limit to climate change due to heat stress. *Proc. Natl. Acad. Sci. USA*, **107**, 9552–9555, https://doi.org/10.1073/pnas.0913352107.

Steadman, R. G., 1979a: The assessment of sultriness. Part I: A temperature-humidity index based on human physiology and clothing science. *J. Appl. Meteor.*, **18**, 861–873, https://doi.org/10.1175/1520-0450(1979)018<0861:TAOSPI>2.0.CO;2.

——, 1979b: The assessment of sultriness. Part II: Effects of wind, extra radiation and barometric pressure on apparent temperature. *J. Appl. Meteor.*, **18**, 874–885, https://doi.org/10.1175/1520-0450(1979)018<0874:TAOSPI>2.0.CO;2.

——, 1984: A universal scale of apparent temperature. *J. Climate Appl. Meteor.*, **23**, 1674–1687, https://doi.org/10.1175/1520-0450(1984)023<1674:AUSOAT>2.0.CO;2.

Stewart, I. D., and T. R. Oke, 2012: Local climate zones for urban temperature studies. *Bull. Amer. Meteor. Soc.*, **93**, 1879–1900, https://doi.org/10.1175/BAMS-D-11-00019.1.

Sun, Y., X. Zhang, F. W. Zwiers, L. Song, H. Wan, T. Hu, H. Yin, and G. Ren, 2014: Rapid increase in the risk of extreme summer heat in Eastern China. *Nat. Climate Change*, **4**, 1082–1085, https://doi.org/10.1038/nclimate2410.

United Nations, 2014: 2014 revision of the World Urbanization Prospects: Highlights. Department of Economic and Social Affairs Population Division, https://www.un.org/en/development/desa/publications/2014-revision-world-urbanization-prospects.html.

Valor, E., V. Meneu, and V. Caselles, 2001: Daily air temperature and electricity load in Spain. *J. Appl. Meteor.*, **40**, 1413–1421, https://doi.org/10.1175/1520-0450(2001)040<1413:DATAEL>2.0.CO;2.

Wang, J., X. Yu, and Y. Zhang, 2017: Statistics show Beijing is getting hotter in summer (in Chinese). *China Meteorological News*, accessed 14 August 2017, http://www.cma.gov.cn/kppd/kppdsytj/201708/t20170814_446240.html.

Wang, K., S. Jiang, J. Wang, C. Zhou, X. Wang, and X. Lee, 2017: Comparing the diurnal and seasonal variabilities of atmospheric and surface urban heat islands based on the Beijing urban meteorological network. *J. Geophys. Res. Atmos.*, **122**, 2131–2154, https://doi.org/10.1002/2016JD025304.

Xie, Z., J. Cui, H. Liu, S. Zhao, J. Sun, C. Hong, and Q. Zeng, 1999: A study on the severe hot weather in Beijing and North China. Part I—Statistics and synoptic case study (in Chinese). *Climatic Environ. Res.*, **4**, 323–333.

Xu, X., F. Chen, S. Shen, S. Miao, M. Barlage, W. Guo, and A. Mahalov, 2018: Using WRF-Urban to assess summertime air conditioning electric loads and their impacts on urban weather in Beijing. *J. Geophys. Res. Atmos.*, **123**, 2475–2490, https://doi.org/10.1002/2017JD028168.

Yang, P., G. Ren, and W. Liu, 2013: Spatial and temporal characteristics of Beijing urban heat island intensity. *J. Appl. Meteor. Climatol.*, **52**, 1803–1816, https://doi.org/10.1175/JAMC-D-12-0125.1.

Yu, M., Y. Liu, Y. Dai, and A. Yang, 2013: Impact of urbanization on boundary layer structure in Beijing. *Climatic Change*, **120**, 123–136, https://doi.org/10.1007/s10584-013-0788-2.

Zhang, L., G. Ren, and Y. Ren, 2015: Identification of urban effect on a single extreme high temperature event (in Chinese). *Climatic Environ. Res.*, **20**, 167–176, https://doi.org/10.3878/j.issn.1006-9585.2014.13175.

Zhao, L., M. Oppenheimer, Q. Zhu, J. W. Baldwin, K. L. Ebi, E. Bou-Zeid, K. Guan, and X. Liu, 2018: Interactions between urban heat islands and heat waves. *Environ. Res. Lett.*, **13**, 034003, https://doi.org/10.1088/1748-9326/aa9f73.